Available online at www.sciencedirect.com
SCIENCE DIRECT®
International Journal of Heat and Fluid Flow 25 (2004) 461–470
International Journal of HEAT AND FLUID FLOW
www.elsevier.com/locate/ijhff

Direct numerical simulation of oblique vortex shedding from a cylinder in shear flow ☆

Jorge H. Silvestrini [a], Eric Lamballais [b,*]

[a] Departamento de Engenharia Mecânica e Mecatrônica, Faculdade de Engenharia, Pontifícia Universidade Católica do Rio Grande do Sul Av. Ipiranga 6681, 90619-900 Porto Alegre—RS, Brazil
[b] Laboratoire d'Etudes Aérodynamiques UMR 6609, Université de Poitiers, Téléport 2—Bd. Marie et Pierre Curie B.P. 30179, 86962 Futuroscope Chasseneuil Cedex, France

Abstract

The vortex dynamics of a shear flow over a circular cylinder is studied by means of Direct Numerical Simulation. Four flow configurations are selected in order to consider the influence of three physical parameters: the vertical extension of the shear zone, the vertical domain size and the shear intensity. Despite the moderate value of the median Reynolds number considered ($Re = 200$), the non-uniform character of the upstream flow leads to the formation of complex Karman streets behind the cylinder for each case. The analysis of the animations shows the occurrence of oblique vortex shedding driven through complex synchronization processes. The shear imposes strong distortions on the Karman vortices and dislocations are regularly observed. The simple observation of the vortical animations does not allow an unambiguous identification of the cellular pattern of vortex shedding. This phenomenon can be more rigorously described by a frequency analysis presented in this paper. It is shown that the main frequency selection is mainly conditioned by a local adjustment of oblique vortex shedding to the upstream velocity. However, due to the preservation of the spatial coherence of the flow, the variation of the main flow frequency occurs by jump along the cylinder axis direction, the distance between two jumps corresponding to the size of a cell. The Karman vortex formation is triggered in the high-speed region of the flow, but paradoxically, the local vortex shedding frequency found in this zone seems to be strongly influenced by the dynamics of the slow part of the flow.

Keywords: Direct numerical simulation; Oblique vortex shedding; Coherent vortices; Immersed boundary method

1. Introduction

Oblique vortex shedding is a common feature in many engineering applications such as marine risers, pillars of offshore platforms and bridges, heat exchangers or ultra-clean protection devices in food industry. In this last case, a recent research on the interactions between a mixing layer and a wake [1] shows the important link between oblique vortex shedding and mean vertical currents behind a circular cylinder oriented in the shear direction associated with the mixing layer (Heitz, 1999; Lamballais and Silvestrini, 2002; Braud et al., 2004a,b). These interactions impose a strong asymmetry in the vertical organization of the wake (i.e. parallel to the cylinder axis). Two dynamically different zones have been clearly identified in these experimental (Heitz, 1999; Braud et al., 2004a,b) and numerical (Lamballais and Silvestrini, 2002) studies: a low-speed wake that follows the behaviour of a conventional wake (produced by a uniform flow) and a high-speed wake that is largely influenced by the vertical currents and highly three-dimensional. Following the main objective of understanding the oblique vortex shedding phenomena, this paper presents numerical results of a shear flow over a circular cylinder. Contrary to these previous studies, where the shear region of the upstream flow was spatially compact (the mixing layer thickness was close to the cylinder diameter), we

☆ Supplementary data associated with this article can be found at doi:10.1016/j.ijheatfluidflow.2004.02.013

* Corresponding author.
E-mail addresses: jorgehs@em.pucrs.br (J.H. Silvestrini), lamballais@univ-poitiers.fr (E. Lamballais).

[1] For an illustration of this specific flow configuration, see Fig. 1 by assuming $L'_y \ll L_y$ and $L'_y \approx D$ where L'_y can be interpreted as the mixing layer thickness.

0142-727X/$ - see front matter © 2004 Elsevier Inc. All rights reserved.
doi:10.1016/j.ijheatfluidflow.2004.02.013

consider here a flow geometry where the vertical extension of the constant shear zone is at least one order of magnitude larger than the cylinder diameter. In this flow configuration, the spatial repartition of the shear effects on the vertical organization of the motions occurs a priori more gradually, in such a way that the links between the main three-dimensional phenomena (non-parallel vortex shedding, secondary vortex creation) should be easier to establish.

For this type of flow, where the cylinder axis is perpendicular to the upstream velocity and vorticity vectors at the same time, interesting results was reported in previous experimental (Maull and Young, 1973; Stansby, 1976; Tavoularis et al., 1987; Woo et al., 1989), numerical (Fröhlich, 2000; Fröhlich et al., 2001; Mukhopadhyay et al., 2002) and theoretical (Noack et al., 1991) studies. The complex nature of this flow geometry was clearly shown through the identification of numerous physical processes related to a specific vortex dynamics where oblique vortex shedding, dislocations and cell formations are the main ingredients. The understanding of these phenomena and their eventual links needs to be improved, especially for practical applications where a fluid control strategy is required. The goal of this study is to examine these mechanisms by taking advantage of the full information offered by Direct Numerical Simulation (DNS). The use of a high spatial resolution allows us to consider flow regimes where three-dimensional motions play an important role with and without the presence of a shear on the upstream flow. This is in contrast to the previous DNS study of Mukhopadhyay et al. (2002) where the Reynolds numbers considered lead to nominally two-dimensional dynamics when a uniform inflow is imposed.

The paper is organized as follows. After an introduction of the flow configuration, some details about the numerical method are briefly presented. Then, visualizations of the instantaneous vortical structures of each simulated flow are shown and analysed. In a second step, quantitative results are presented through a frequency analysis in order to better understand the physical mechanisms responsible of the local selection of vortex shedding processes.

2. Flow configuration and parameters

A shear flow over a circular cylinder of diameter D is considered in a Cartesian frame of reference $\mathscr{R} = (0; x, y, z)$ where the velocity components are noted (u_x, u_y, u_z). The cylinder axis is oriented along the vertical direction y at the intersection between the streamwise position x_{cyl} and the spanwise one $z = 0$ (see Fig. 1). At the inflow section, the constant shear is aligned in y-direction and extends over a zone $-L'_y/2 < y < L'_y/2$.

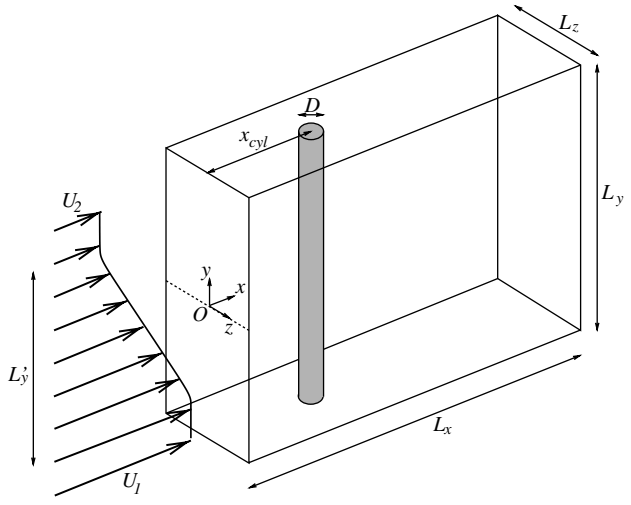

Fig. 1. Schematic view of the flow configuration.

Outside this zone, two streams of constant velocities U_1 (for $y < -L'_y/2$) and U_2 (for $y > L'_y/2$) are imposed, with $U_1 > U_2$. The inflow velocity profile $U(y)$ at $x = 0$ is given by

$$U(y) = \frac{U_1 + U_2}{2} + \frac{U_2 - U_1}{12} \times \frac{D}{L'_y}\left\{ \ln\left(\frac{\cosh\left[\frac{6}{D}\left(y + \frac{L'_y}{2}\right)\right]}{\cosh\left[\frac{6}{D}\left(y - \frac{L'_y}{2}\right)\right]} \right) \right\} \quad (1)$$

without any additional perturbations (steady inflow condition). This profile allows us to consider a constant shear flow extending over a wide region while preserving the free-slip conditions imposed at $y = \pm L_y/2$. Note that contrary to the generic case of a cylinder wake due to a uniform upstream flow, the present flow configuration does not allow the system to be considered as an infinitely long cylinder (well represented by the use of a periodic condition) due to the necessarily limited extent of the shear region of the upstream flow.

The presence of free-slip walls, equivalent to mirror conditions assumed at $y = \pm L_y/2$, imposes a kinematic blocking associated with the condition

$$u_y(x, \pm L_y/2, z) = 0. \quad (2)$$

As a first consequence, even in the case without shear ($U_1 = U_2$), this blocking breaks the homogeneous character of the flow with respect to the y-direction. The y-dependence of turbulent statistics is significant near $y = \pm L_y/2$ where the y-component of fluctuating velocity needs to collapse in order to verify the condition (2). Despite this effect, considering the case of a conventional wake due to a uniform flow, Lamballais and Silvestrini (2002) have shown that the main features of the wake dynamics were preserved when free-slip walls were used instead of periodic boundary

Table 1
Flow configurations and simulation parameters

Case	$L_x \times L_y \times L_z$	$n_x \times n_y \times n_z$	L'_y	β
OW1	$22D \times 12D \times 12D$	$397\times97\times216$	$10D$	0.1
OW2	$22D \times 24D \times 12D$	$397\times193\times216$	$10D$	0.1
OW3	$22D \times 48D \times 12D$	$397\times385\times216$	$10D$	0.1
OW4	$22D \times 48D \times 12D$	$397\times385\times216$	$40D$	0.025

conditions, especially concerning the vortex shedding that was found to be parallel for both cases. In this sense, the oblique mode selection found in this work can be viewed as an intrinsic feature of the flow under study rather than a secondary consequence of the set of boundary conditions used in y-direction. Moreover, by choosing the condition $L_y \gg L'_y$, it is possible to reduce the blocking effect while distinguishing three basic flows in the computational domain: a high-speed wake ($-L_y/2 < y < -L'_y/2$), a skewed-wake ($-L'_y/2 < y < L'_y/2$) and a low-speed wake ($L'_y/2 < y < L_y/2$). Note finally that a periodic boundary condition is imposed in z-direction.

DNS of a shear flow over a circular cylinder was performed by considering two shear parameters $\beta = 0.1$, 0.025 defined by

$$\beta = -\frac{D}{U_c}\frac{dU}{dy} \tag{3}$$

where $U_c = (U_1 + U_2)/2$ is the median velocity. Note that both couples of parameters (β, L'_y) considered here yields $U_1 = 3U_c/2$ and $U_2 = U_c/2$. The corresponding Reynolds number ($Re = U_c D/\nu$) is 200, the local Reynolds number associated with the inflow velocity profile (1) varying from $Re_2 = U_2 D/\nu = 100$ to $Re_1 = U_1 D/\nu = 300$. For all calculations presented in this paper, the cylinder is located at $x_{cyl} = 7D$.

In what follows, four DNS' are presented (see Table 1). For three calculations, a different vertical dimension of the domain L_y is used while maintaining constant the extension of the constant shear zone $L'_y = 10D$. The comparison between these three cases allows us to examine the effects of the flow conditions in the neighbourhood of the shear region limits $y = \pm L'_y/2$, where free-slip walls (case OW1) or low- and high-speed wakes (cases OW2 and OW3) can be present. In the fourth case OW4, the shear intensity is moderate with a shear zone extended to $L'_y = 40D$.

3. Numerical methodology

The incompressible Navier–Stokes equations are directly solved on a computational grid of $n_x \times n_y \times n_z$ points in non-staggered configuration. Sixth-order compact centred difference schemes are used to evaluate all spatial derivatives, except near the in- and outflow boundaries where single sided schemes are employed for the x-derivative calculation. Time integration is performed with a third-order low-storage Runge–Kutta method. For more details about the numerical code, see Lardeau et al. (2002) and Silvestrini and Lamballais (2002).

Despite its fundamental character, the flow geometry considered in this study presents some difficulties linked to the requirements of DNS in terms of accuracy and computational cost. Near the body, a cylindrical grid is a priori well suited, but further downstream in the flow, the increase of azimuthal mesh size associated with this type of grid is a drawback. In order to avoid the difficulties associated with more sophisticated grids (loss of accuracy due mesh distortions, increase of the computational cost, ambiguity associated with the definition of an optimal grid), we use here an "immersed boundary method". More precisely, the presence of the cylinder is modelled with the aid of a feedback forcing (Goldstein et al., 1993) that "freezes" the fluid in the body region. In a previous study (Lamballais and Silvestrini, 2002), we have shown that this method can be combined with a code based on high-order finite difference schemes to produce reliable results in the case of a conventional cylinder wake, especially for the prediction of the Strouhal number, the mean velocities, the turbulent stresses or the vortical organization of the flow. Here, we use the same numerical methodology with similar spatial and temporal resolutions (by taking the Reynolds number into account), in such a way that equivalent accuracy can be expected for the present results (see Table 1 for additional details on simulation parameters).

4. Results

4.1. General view of the flows

In first analysis, the physical mechanisms governing the dynamics of the present flows can be shown qualitatively using visualization. Naturally, the choice of the technique used to identify the various physical processes introduces a significant part of subjectivity. In this section, we are interested in the dynamics of Coherent Vortices (CV). Following the CV definition of Lesieur (1997), we consider here the "vortical activity" of the flows through the vorticity concentration, a necessary

but not sufficient condition for a vortex to exist. Note that more refined techniques for the vortex identification have been developed like the Q or λ_2 criteria (Hunt et al., 1988; Jeong and Hussain, 1995; see also Schoppa and Hussain, 1996 and Dubief and Delcayre, 2000 for a review). These two quantities are better suited to isolate a vortex core by avoiding the detection of vorticity sheets and high shear. Here, we prefer to present visualizations based on vorticity in order to better observe the early formation of Karman structures through the roll-up of the vorticity sheets just behind the cylinder.

If a simple isosurface of vorticity is presented, the y-dependence of vorticity levels leads to a discrimination between the CV in the high- and low-speed regions of the flow. For instance, the selection of an isosurface of high vorticity yields a vortical detection only in the fast zone of the flow. Even if the visualization of a moderate vorticity level allows a detection of CV in the full domain, it leads to a loss of clarity in the picture obtained in the high-speed region. This behaviour is obviously a consequence of the vorticity generation by the cylinder which scales, in first approximation, on the upstream velocity $U(y)$ given by (1) and the cylinder diameter D. For this reason, we present in Fig. 2 various perspective views of a specific quantity corresponding to the vorticity modulus (the root mean square of twice the enstrophy) normalized by $U(y)$ and D. Using this normalization, a well-balanced view of the structural organization of the flow can be obtained. Note that the choice of this normalization is only used to clarify the global views of the flows (especially the animations). We verified that all qualitative comments given in this paper about the vortex dynamics are preserved when the conventional vorticity is directly visualized using a specific threshold for the observation at a given y-location.

The pictures in Fig. 2 were taken at the end of each calculation. The animations [2] are presented for a temporal sequence of $T = 78D/U_c$. Note that all results presented in this paper were obtained after the transient time had elapsed during which statistically steady conditions are established. The views presented in Fig. 2 illustrate well the complexity of this type of flow. In all cases, oblique Karman vortices can be observed behind the cylinder. For the present visualization technique, we consider that a tubular shape of the isosurface indicates the presence of a vortex. At this preliminary stage of the flow analysis, it is useful to notice that the organization of the oblique Karman vortices arises from two cumulative effects: (i) the slantwise nature of the vortex shedding just behind the cylinder (ii) the re-orientation of Karman vortices by a mechanism of differential transport in the shear region of the flow further downstream.

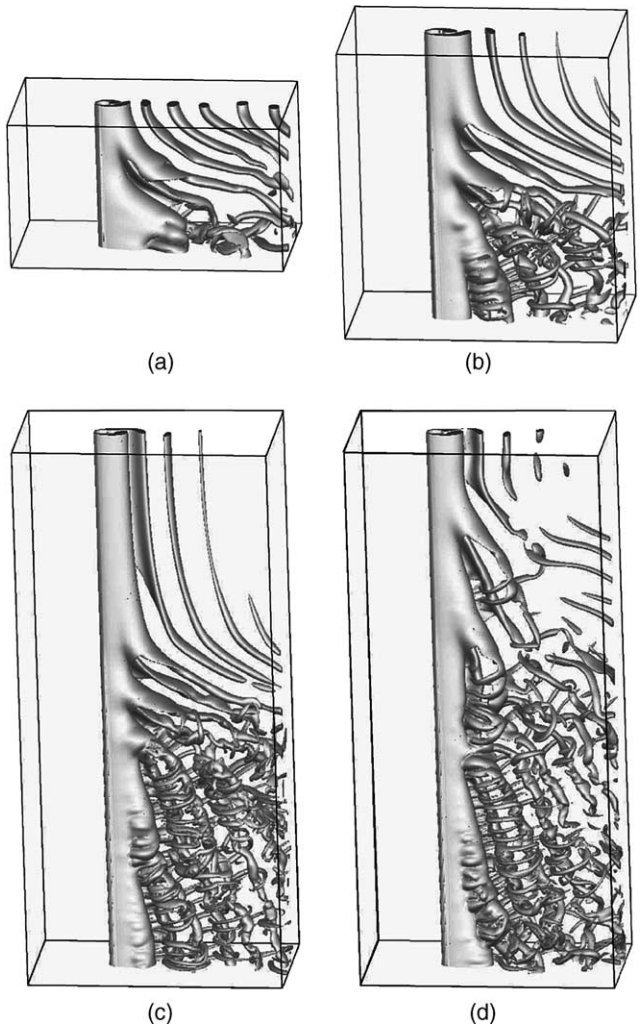

Fig. 2. Perspective views showing isosurfaces of $\omega D/U(y)$ where ω is the vorticity modulus $\left(\omega = \sqrt{\omega_x\omega_x + \omega_y\omega_y + \omega_z\omega_z}\right)$ and $U(y)$ is given by (1): (a) Case OW1, (b) Case OW2, (c) Case OW3, (d) Case OW4.

The primary origin of the oblique vortex structure is related to the slantwise vortex shedding itself. It is well known that non-parallel vortex shedding can occur even if upstream conditions correspond to a uniform flow in an extended region. In particular, it was shown clearly that end conditions for a finite cylinder are able to determine the vortex shedding mode (parallel/oblique selection, see Williamson, 1996 and Mittal, 2001). In the present flow configuration, the oblique vortex shedding is obviously related to the presence of the upstream shear. However, it is worth noting that the extent of regions where oblique vortex shedding is found does not necessarily correspond to the extent of the shear region. Hence, the preservation of oblique vortex shedding in the subdomain $y \in [-L_y/2, -L'_y/2]$ is not a priori expected for the case OW3 since in this region, the upstream flow is constant over a large y-extension of

[2] Animations (mpeg format) 1–4 are available in the online version of this paper. Animation 1: Case OW1; animation 2: Case OW2; animation 3: Case OW3; animation 4: Case OW4.

$L_y/2 - L'_y/2 = 19D$. In contrast, the return to a conventional two-dimensional vortex shedding mode can be clearly observed in the low-speed region of the OW3 flow, as shown by the view 2(c). The analysis of animations illustrates very well the physical mechanisms associated with the oblique vortex shedding. In particular, it can be observed that the formation of Karman vortices is triggered preferentially in the high-speed region of the flow and is propagated towards positive y-coordinates. From this view, the angle of the vortex shedding appears to be conditioned by the characteristic speed of this vortex shedding propagation in y-direction. This driving of the vortex dynamics near $y \approx -L_y/2$ suggests a strong receptivity of the flow dynamics in this region, a property that could be interesting in the context of flow control.

Further downstream, in regions where the shear is significant ($-L'_y/2 < y < L'_y/2$), the obliqueness of the wake structures is increased by a simple convective mechanism. Due to the high value of the shear parameter β, the obliqueness of large-scale vortices is very pronounced in the shear region for the cases OW1, OW2 and OW3. Further downstream, these structures twist alternatively in a clockwise and counter-clockwise direction. In the simulation OW4 for which the parameter β is more moderate, the oblique character of the vortex shedding is logically less pronounced in the shear region. However, animations show clearly a continual re-orientation of the Karman vortices as they are convected downstream. In an idealized constant-shear flow

$$U(y) = U_c(1 - \beta y/D), \tag{4}$$

it is easy to show that the angle $\theta(t)$ between a Lagrangian line and the shear axis y follows the temporal law

$$\theta(t) = \tan^{-1}\left(\tan\theta_0 + \frac{U_c\beta}{D}t\right) \tag{5}$$

where θ_0 is the initial angle at $t = 0$. Following this very simplified view, it is natural to expect that the downstream transport of Karman vortices in the shear region tends to increase their obliqueness until they are aligned with the longitudinal direction. This second mechanism of slantwise vortex formation is illustrated in Fig. 4 where the main directions of some Karman vortices are approximately indicated by lines. In this figure, the difference between cases OW3 and OW4 is clear. For the OW3 case, in the high-speed region of the flow (locally free of shear), the Karman structures form obliquely and keep their initial directions further downstream. In contrast, the obliqueness of Karman vortices continuously increases with x for the OW4 case, as it can be expected from convection effects. Naturally, this re-orientation mechanism by transport is more efficient in highly sheared regions, as it can be observed in the four cases (see Fig. 2).

Due to high values of the shear β and its vertical extension L'_y considered here, the occurrence of Karman vortices crossing the complete computational domain in y-direction is never observed. The more extended oblique vortices are found in the cases OW3 and OW4, in the high-speed region as well as in the low-speed region of the flow.

4.2. Analysis of 3D motions

Before describing the spatial organization of 3D motions, it is useful to clarify the nature of the four flow configurations considered here. As already stressed in a previous section, it is possible to define a local Reynolds number $Re_l(y) = U(y)D/\nu$ associated with the inflow velocity profile. In the four cases considered here, Re_l covers the same range $Re_l(y) \in [Re_2, Re_1]$ with $Re_2 = U_2D/\nu = 100$ to $Re_1 = U_1D/\nu = 300$. In a conventional wake behind a cylinder ($U_1 = U_2$), the Reynolds number dependence of the flow dynamics is considerable in the range $Re \in [100, 300]$. Schematically, three typical flow regimes can be distinguished (Williamson, 1996). When $100 < Re < 190$, a purely two-dimensional vortex shedding occurs. Above this critical value, three-dimensional motions appear. In the transition regime $190 < Re < 260$, the 3D instability leads to the formation of longitudinal vortices spaced in y-direction at a typical wavelength of around 3–4 diameters. These structures are related to an instability called mode A. From $Re \approx 230$, this mode is gradually replaced by the mode B instability that leads to the appearance of a second class of 3D structures of finer scale. In the last range $260 < Re < 300$ covered in the present flow configuration, mode B becomes dominant, the main topological change of the wake being related to the wavelength selection of longitudinal structures (stretched between Karman vortices) that are spaced by about only one diameter.

If the present flow configuration is idealized as a set of independent 2D wakes of varying Reynolds number (by neglecting vertical motions), three flow regimes are expected to coexist in the same computational domain. The observation of each visualization presented in Fig. 2 shows that this somewhat oversimplified view is basically recovered for cases OW2 and OW3 as far as the two-dimensional behaviour of the flow in the low-speed region and the appearance of the mode B instability in the high-speed region are concerned. The transition regime is quite delicate to identify for the case OW4, while being indistinguishable for the other cases. For the flows OW1 and OW2, the effects of free-slip walls ($y = \pm L_y/2$) do not allow an easy identification of local flow regimes. However, in all flow configurations, strong secondary vortices are created between the distorted Karman

vortices in the high-speed region of the flow. Note, however, that for the case OW1, the 3D organization of the flow near the lower free-slip wall ($y = -L_y/2$) does not allow us to identify formally a vortex shedding process. Finally, it is interesting to observe that in regions where Karman vortices are strongly inclined (cases OW1, OW2, OW3), a very unusual vortical topology is obtained where secondary vortices are mainly oriented in the vertical direction contrary to the conventional case where equivalent structures are stretched in the streamwise direction.

4.3. Cellular pattern of vortex shedding

Even if an adjustment of the vortex shedding frequency to the local upstream velocity $U(y)$ can be expected, the preservation of the coherence of the motion in y-direction prevents this process to be purely local. Schematically, the coherence of the vortices tends to maintain a phase relation in y-direction over a significant physical length. The critical value of this length corresponds to the size of a cell where, by definition, the vortex shedding frequency should be constant. The formation of cells in the vortex shedding behind a body in a shear flow was already noted in previous studies (Maull and Young, 1973; Stansby, 1976; Tavoularis et al., 1987, Woo et al., 1989; Fröhlich, 2000; Fröhlich et al., 2001; Mukhopadhyay et al., 2002). A simple theoretical model was proposed by Noack et al. (1991) for this phenomenon at low Reynolds number ($100 < Re < 160$). For the present results, a simple observation of the animations does not allow us to identify unambiguously the cell formation mechanisms. For the case of moderate shear (OW4), oblique Karman-like vortices of moderate span can be identified, but it is delicate to locate formally the corresponding cells. Despite this difficulty, it is interesting to observe that periodically, a phase breaking occurs in a dislocation process in agreement with previous observations. In the present results, dislocations can be clearly observed on animations through the identification of vortices that are torn by the main flow. For the case OW1, only one cell can be clearly identified, the 3D motions near the lower free-slip wall ($y = -L_y/2$) being not organized enough to allow us to distinguish any vortex shedding process. For the cases OW2 and OW3, two cells can be easily identified outside the shear region. These two cells seem to synchronize the flow in the central region $-L'_y/2 < y < L'_y/2$ where the occurrence of highly 3D motions prevents the clear identification of other cells.

4.4. Frequency analysis

A rigorous identification of the number and size of cells needs to consider quantitatively the spatial repartition of the main frequencies governing the flow dynamics. For this purpose, a set of temporal data was stored for several x and y locations. The length of the time series used is $T = 114D/U_c$. The frequencies f associated with each time series was obtained by means of Fourier analysis based on conventional FFT. Here, we present only transverse velocity data u_z corresponding to the streamwise position $x - x_{cyl} = 2D$ in the symmetric plane $z = 0$. In order to show the vertical variability of the flow, typical time series and their associated spectra (vs. the dimensionless frequency fD/U_c) are presented by covering the full extent of the

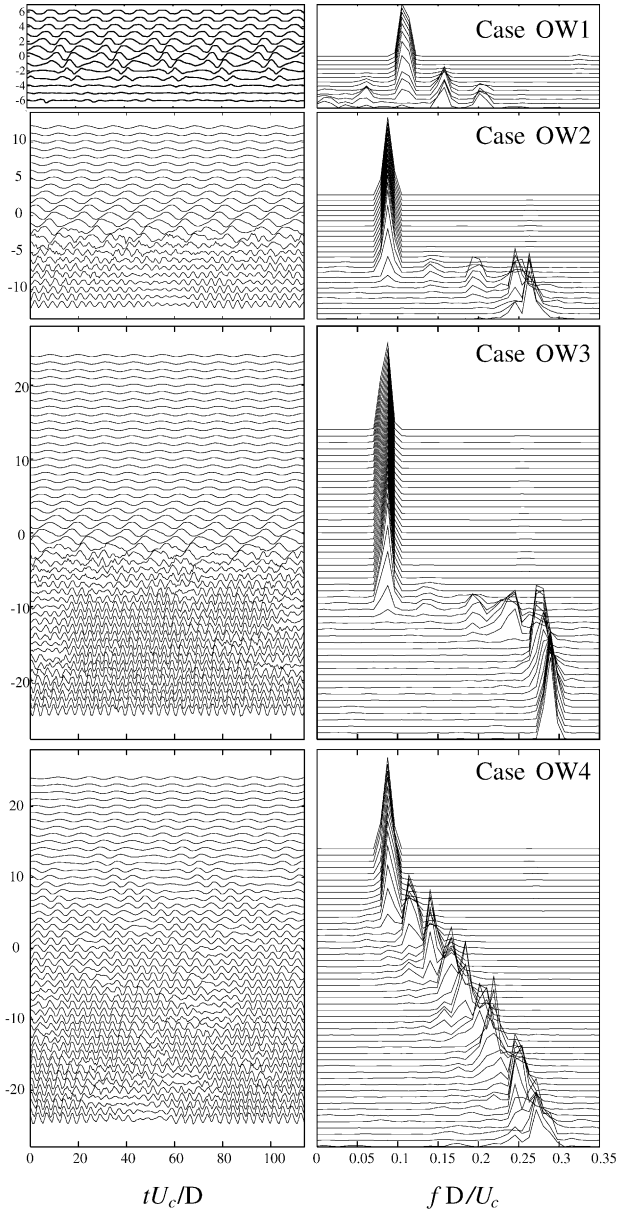

Fig. 3. Vertical variation from $y = -L_y/2$ to $y = L_y/2$ of time series (left) and their frequency spectra (right) of transverse velocity $u_z(x_{cyl} + 2D, y, 0, t)$. The power spectra density vertical axe is on an arbitrary scale. Curve for each vertical location (where y/D takes an integer value) is plotted with a successive offset.

computational domain in y-direction. The four cases OW1, OW2, OW3 and OW4 are presented in Fig. 3.

Let us first consider the main frequencies associated with the locally constant high- and low-speed flows of velocity U_1 and U_2, respectively. These two frequencies can be deduced by the examination of spectra that admit two marked peaks near the locations $y = \pm L_y/2$. In order to establish a link between these values and the one corresponding to a conventional wake, it is convenient to define the two local Strouhal numbers $St_1 = fD/U_1$ and $St_2 = fD/U_2$ where f is the frequency under study. For cases OW2, OW3 and OW4, a similar value is found in the low-speed region of the flow with $St_2 \approx 0.16$. This value is close to the one obtained for a conventional wake at $Re = 100$ (Williamson, 1996). For the case OW1, the value given by spectra peaks near $y \approx L_y/2$ is significantly increased with $St_2 = 0.22$. This increase of the vortex shedding frequency seems to be an effect of the upper free-slip wall ($y = L_y/2$) that is very close to the shear region due to the moderate extension of the computational domain in y-direction. In the high-speed region, the presence of the lower free-slip wall ($y = -L_y/2$) influences more strongly the frequency selection of the vortex shedding. Hence, we obtain $St_1 \approx (0.17, 0.19, 0.18)$ for cases (OW2, OW3, OW4) respectively. These values are lower than those for a conventional wake at $Re = 300$ where $St = 0.2$ is a well accepted value. Note that the decrease of St_1 is more pronounced when L'_y is close to L_y.

The examination of the vertical variation of spectra presented in Fig. 3 shows that the main frequency selection is strongly affected by the shear parameter β and by the ratio L'_y/L_y. For the case OW1, several peaks are clearly visible. Super- and sub-harmonic frequencies can be identified at the same y-location, especially in the high-speed region where we cannot observe a clear dominant frequency, confirming the idea that the vortex shedding is strongly destructured. For the other cases OW2, OW3 and OW4, at each y-location, the domination of a single frequency is more marked, suggesting the occurrence of a regular vortex shedding process. An interesting point is that the main frequency varies discontinuously from a y-location to another. This behaviour can be related to the vertical coherence of vortex shedding that is organized, as already discussed previously, in cells distributed along the cylinder.

In order to better analyse the vortex shedding frequency selection, let us consider more specifically the cases OW3 and OW4. Fig. 4 presents views comparing visualizations and y-locations of main frequencies. In addition, an idealized frequency profile is plotted. This reference frequency f_i, local by nature, is estimated by

$$f_i(y) = \frac{U(y)\cos\theta}{D}\left(0.212 - \frac{4.5v}{U(y)D}\right) \tag{6}$$

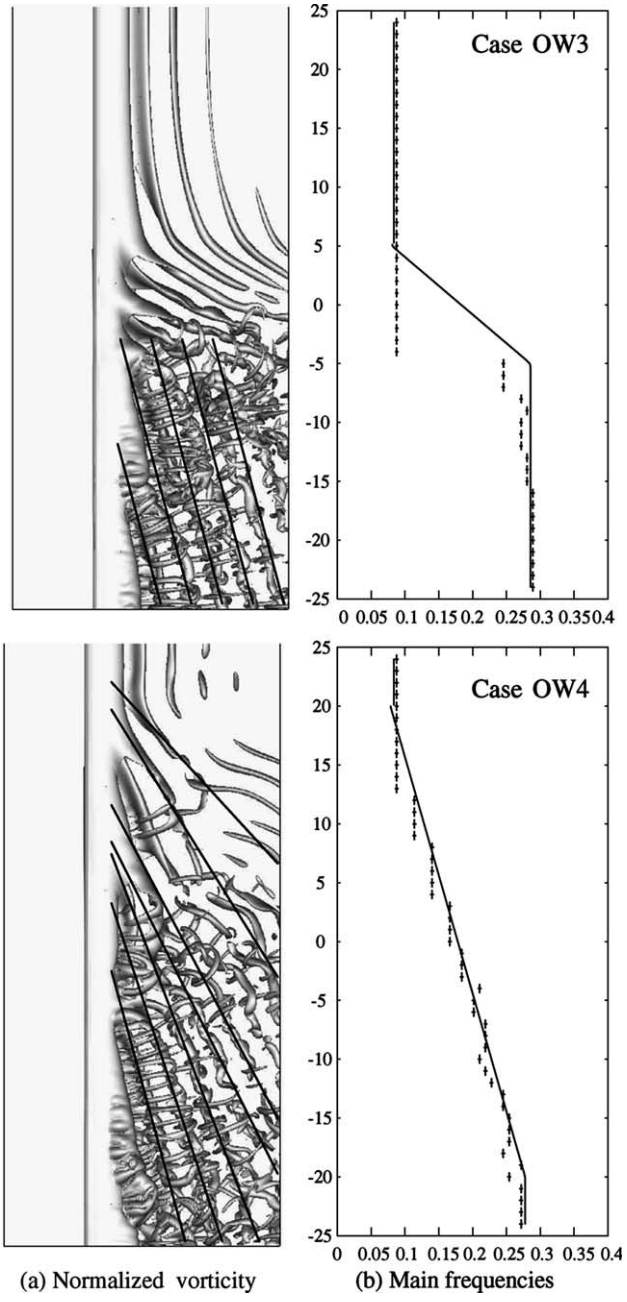

Fig. 4. Comparison of instantaneous visualizations and main frequency profiles. (a) Same visualization than for Fig. 2 in side view, (b) vertical variation of the main frequencies corresponding to spectra maximums presented in Fig. 3 (+: measured frequencies; –: profile of the idealized frequencies f_i given by relation (6)).

This relation is simply a local adaptation of Roshko's empirical law $St = 0.212 - 4.5/Re$ including the correction by the cosine of the angle formed by the oblique vortices just behind the cylinder. In the context of a conventional cylinder wake, this correction was demonstrated to be useful in predicting the reduction of the shedding frequency accurately when oblique shedding appears (Williamson, 1996; Mittal, 2001). Here, we crudely approximate the angle θ as zero in the slowest

region of the flow ($Re \approx 100$) where the vortex shedding is locally parallel, whereas in the rest of the domain, we assign to this angle a constant value with $\theta \approx 15$ and $\theta \approx 20$ for the cases OW3 and OW4 respectively, in agreement with the visual mean inclination of the vortices observed in animations just behind the cylinder. The comparison between the idealized frequency profile and the frequencies measured emphasizes very well the occurrence of synchronization mechanisms preserving the vertical coherence of the flow. Outside of the shear region, for both cases OW3 and OW4, a quite good agreement is obtained between the measured frequencies and the idealized ones. In contrast, the selection of the main frequency can strongly deviate from its idealized estimation in the sheared zone, especially for the case OW3 in the low-frequency range. For this case, the frequency selection in the shear regions seems to be mainly conditioned by the vortex shedding on the low-speed side of the flow without any local adjustment on the mean velocity $U(y)$. Near $y = -L'_y/2$, the main frequency suddenly returns near its idealized estimation through a considerable jump (see Fig. 4). For lower y, nominally three plateau values can be observed, suggesting again a cellular structure of the vortex shedding in this region of the flow. Similarly, for the case OW4, nominally nine cells can be identified, but it should be recognized that in the high-speed part of the flow, due to the highly 3D motions, the location of the cell boundaries cannot be determined unambiguously. Despite this reservation, the variation by jump of the main frequency which maintains a local Strouhal number close to the conventional cylinder wake is well recovered for OW4. Moreover, the large number of cells noticed is consistent with the observation that this case leads to numerous vortex dislocations, as clearly shown by the animations.

A last comment can be made about the intermittent nature of u_z-time signals presented in Fig. 3. A global examination of these time series shows clearly that for the four cases considered here, the vortex shedding process can be very irregular outside regions where the inflow velocity $U(y)$, and its associated local Reynolds number $Re_l(y)$, remain moderate. For instance, in the case OW4, in the range $5D < y < 12D$, the vortex shedding seems to be periodically almost interrupted. The visual examination of the neighbourhood of each signal shows that the corresponding defects seem to propagate from the low-speed region of the flow to the high-speed one with a typical phase-speed estimated crudely by $V \approx 0.4U_c$. This phenomenon is qualitatively consistent with previous observations of Fröhlich (2000) and Fröhlich et al. (2001) who studied these mechanisms in details through wavelet analysis of LES data at higher Reynolds number ($Re = 6250$) for an intermediate shear $\beta = 0.04$. In the present cases (OW1, OW2, OW3), defects in velocity undulation can be also recovered, confirming the intermittent character of vortex shedding due to a shear flow. Note that the principle of propagation of these defects towards the high-speed region seems to be conserved for each case. However, for a more rigorous analysis of these phenomena, it is clear that the temporal sequence of present signals must be considerably extended in order to increase the number of events, this number being here too limited.

5. Discussion and conclusion

In this work, the complex nature of the vortex dynamics created by a shear flow over a cylinder is clearly shown. The examination of graphical animations emphasizes the crucial role played by Karman vortices that undergo strong distortions due to the shear of the main flow. The more evident effect is the release of slantwise vortex shedding for the four configurations considered here.

However, the oblique vortex shedding cannot occur along the full span of the cylinder due to the significant velocity difference between the end conditions. Schematically, two basic trends can be contrasted. The first one consists in a local adjustment of the vortex shedding frequency $f(y)$ to the local upstream velocity $U(y)$ by limiting the deviation of the local Strouhal number $St_l(y) = f(y)D/U(y)$ from its value for a conventional wake. This local selection, leading to high frequencies in the high-speed region of the flow (of highest Reynolds number $Re_l(y)$), is well recovered in the present study if the angle of the oblique vortex shedding is taken into account (use of the cosine correction in the empirical relation (6)).

Naturally, such a local adjustment of the frequency cannot be purely local in order to maintain the coherence of the flow vortices along the y-direction. The preservation of this coherence is the second mechanism contrasting the first one. It can be observed qualitatively by vortex visualization and quantitatively by the identification of the deviation of the frequencies measured from their idealized estimation (comparisons presented in Fig. 4 for the cases OW3 and OW4). The discontinuous variation of the frequencies along the y-direction exhibits the cellular structure of the vortex shedding in the sheared region of the flow. The size of the cells probably depends on the extension and the intensity of the shear. It could be interesting to perform additional calculations in order to identify more clearly the relevant scaling parameters for this length selection.

Further downstream in the flow, the differential transport of the Karman vortices leads to distorted vortex structures with the occurrence of dislocations (phase breaking, tearing of vortices). The dislocation phenomenon can be better understood with the help of a model based on the differential twisting of a vortex tube by a constant shear flow. Hence, let us consider an ob-

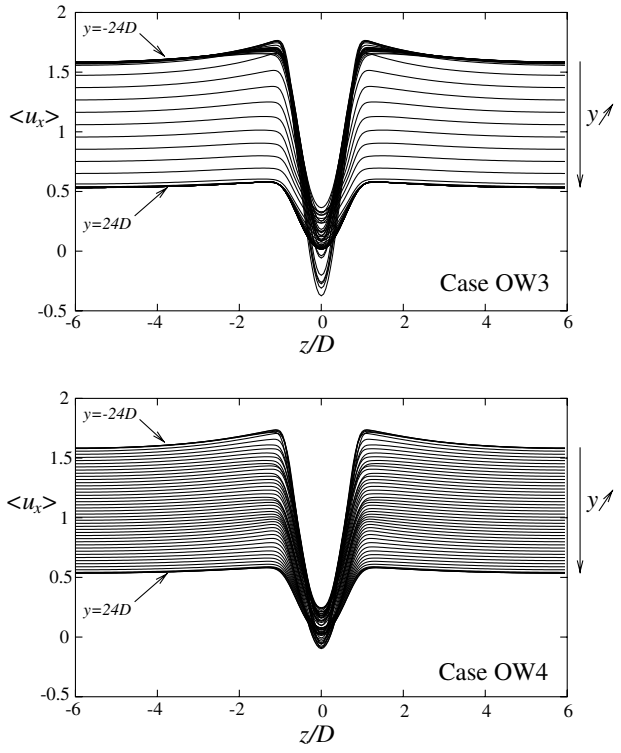

Fig. 5. Mean streamwise velocity profiles $\langle u_x \rangle$ at $x - x_{\mathrm{cyl}} = 2D$ from (top to bottom) $y = -24D$ to $y = 24D$ at each D.

lique detached vortex tube convected downstream by a 3D wake flow similar to the present configuration. To better illustrate the flow behind the cylinder, streamwise mean velocity profiles in various vertical locations are presented in Fig. 5 for cases OW3 and OW4. The shear in the z-direction introduced by the cylinder (through the no-slip condition) leads to wake profiles with a velocity deficit that scales on $U(y)$ in a first analysis. Schematically, the velocity difference associated with the high-speed wake (for $-L_y/2 < y < -L'_y/2$) is increased by a factor of U_1/U_2 with respect to the one obtained in the low-speed wake (for $L'_y/2 < y < L_y/2$). These velocity differences induce a hierarchical distribution of vorticity in the detached vortex tube. As a consequence, the vortices twist in a differential way depending on the vertical location, turning round faster in the high-speed wake than in the low-speed wake. This mechanism makes the vortex tube take the form of a "corkscrew". "Corkscrew curl" vortex-tube can be easily identified in the shear zone of all simulations (see animations and Fig. 2).

The question that now arises is: can the oblique vortex tube preserve its form as a "one-piece tube" while being twisted with different levels of vorticity? The answer seems to be related to the choice of the β parameter and, probably, to the vertical dimension of the shear zone (given here by L'_y). For low values of β, the differential twisting phenomenon may not be so intense (corresponding to low levels of difference velocity in the shear layer) and the vortex tube may preserve its form. On the other hand, if β is higher than a critical value, the differential twisting phenomenon may break the vortex by torsion and produce a "two-piece tube". It is tempting to associate this vortex tube breakdown to the occurrence of dislocation phenomena. The vortical animations of cases OW3 and OW4 suggest such a link. Once again, additional calculations on larger computational domains could be useful to establish more clearly the mechanisms driving the typical frequencies and spatial lengths of dislocations.

Finally, let us mention the ambiguity of any analysis in terms of causal relationship. For instance, the direct observation of animations shows clearly that the vortex shedding is triggered in the high-speed region of the flow. The formation of Karman structures appears to be a periodic phenomenon that propagates towards the low-velocity zone, the propagation length being limited by the breakdown processes due to the local frequency adjustment already discussed above. This mechanism suggests that the high-speed region is able to synchronize the low-speed one. However, when the same phenomenon is analysed through frequency analysis, the temptation is to draw the opposite conclusion. For instance, in the case OW3, we observe clearly that the deviation from the idealized frequency is mainly conditioned by the low-speed flow dynamics. To summarize, the oblique character of vortices suggests a synchronization of the low-speed flow by the high-speed one, while the frequency selection leads to the reverse interpretation. The simplified physical model conciliating these two views remains to be established.

Acknowledgements

The present calculations and visualizations were carried out at the IDRIS, the computational centre of the CNRS. We are grateful to Thierry Goldmann (IDRIS) for its precious help in producing the graphical animations. Francis Boissonneau, Jean-François Largeau and Valérie Lefeuvre are also gratefully acknowledged. This study was partially supported by the CNRS.

References

Braud, C., Heitz, D., Arroyo, G., Delville, J., 2004a. Analysis of the wake mixing-layer interaction using multiple plane PIV and 3D classical POD. Exp. Fluids, in press.

Braud, C., Heitz, D., Arroyo, G., Perret, L., Delville, J., Bonnet, J.-P., 2004b. Low-dimensional analysis, using POD, for two mixing layer–wake interactions. Int. J. Heat Fluid Flow, this issue.

Dubief, Y., Delcayre, F., 2000. On coherent-vortex identification in turbulence. J. Turbul. 1, 011.

Fröhlich, J., 2000. LES of vortex shedding past circular cylinders. In: Proceedings of ECCOMAS 2000, Barcelona, 11–14 September.

Fröhlich, J., Rodi, W., Bertoglio, J.P., Bieder U., Touil, H., 2001. Large eddy simulation of flow around circular cylinders on structured and unstructured grids, II. In: Hirschel, E.H. (Ed.), Notes on Numerical Fluid Mechanics, vol. 75, pp. 231–249.

Goldstein, D., Handler, R., Sirovich, L., 1993. Modeling a no-slip boundary condition with an external force field. J. Comp. Phys. 105, 354–366.

Heitz, D., 1999. Etude expérimentale du sillage d'un barreau cylindrique se développant dans une couche de mélange plane turbulente. Ph.D. thesis, Université de Poitiers.

Hunt, J.C.R., Wray, A.A., Moin, P., 1988. Eddies, stream and convergence zones in turbulent flows. CTR S88, 128.

Jeong, J., Hussain, F., 1995. On the identification of a vortex. J. Fluid Mech. 285, 69–94.

Lamballais, E., Silvestrini, J., 2002. Direct numerical simulation of interactions between a mixing layer and a wake around a cylinder. J. Turbul. 3, 028.

Lardeau, S., Lamballais, E., Bonnet, J.P., 2002. Direct numerical simulation of a jet controlled by fluid injection. J. Turbul. 3, 002.

Lesieur, M., 1997. Turbulence in fluids, third ed. Kluwer Academic Publishers.

Maull, D.J., Young, R.A., 1973. Vortex shedding from bluff bodies in a shear flow. J. Fluid Mech. 60, 401–409.

Mittal, S., 2001. Computation of three-dimensional flows past circular cylinder of low aspect ratio. Phys. Fluids 13 (1), 177–191.

Mukhopadhyay, A., Venugopal, P., Vanka, S., 2002. Oblique vortex shedding from a circular cylinder in linear shear flow. Comp. Fluids 31, 1–24.

Noack, B.R., Ohle, F., Eckelmann, H., 1991. On cell formation in vortex streets. J. Fluid Mech. 227, 293–308.

Schoppa, W., Hussain, F., 1996. New aspects of vortex dynamics relevant to coherent structures in turbulent flows. In: Bonnet, J.P. (Ed.), Eddy Structure Identification. Springer-Verlag, pp. 61–143.

Silvestrini, J.H., Lamballais, E., 2002. Direct numerical simulation of wakes with virtual cylinders. Int. J. Comp. Fluid Dynam. 16 (4), 305–314.

Stansby, P.K., 1976. The locking-on of vortex shedding due to the cross-stream vibration of circular cylinders in uniform and shear flows. J. Fluid Mech. 74, 641–665.

Tavoularis, S., Stapountzis, H., Karnik, U., 1987. Vortex shedding from bluff cylinders in strongly sheared turbulent streams. J. Wind Eng. Ind. Aerodynam. 26, 165–178.

Williamson, C.H.K., 1996. Vortex dynamics in the cylinder wake. Ann. Rev. Fluid Mech. 28, 477–539.

Woo, H.G.C., Cermak, J.E., Peterka, J.A., 1989. Secondary flows and vortex formation around a circular cylinder in constant-shear flow. J. Fluid Mech. 204, 523–542.